Electrolytes

Locally Concentrated Ionic Liquid Electrolytes Enabling Low-Temperature Lithium Metal Batteries

Xu Liu, Alessandro Mariani, Thomas Diemant, Xu Dong, Po-Hua Su, and Stefano Passerini*

Abstract: Lithium metal is a promising anode material for next-generation high-energy-density batteries but suffers from low stripping/plating Coulombic efficiency and dendritic growth particularly at sub-zero temperatures. Herein, a poorly-flammable, locally concentrated ionic liquid electrolyte with a wide liquidus range extending well below 0°C is proposed for low-temperature lithium metal batteries. Its all-anion Li^+ solvation and phase-nano-segregation solution structure are sustained at low temperatures, which, together with a solid electrolyte interphase rich in inorganic compounds, enable dendrite-free operation of lithium metal anodes at $-20°C$ and $0.5\,mA\,cm^{-2}$, with a Coulombic efficiency of 98.9%. As a result, lithium metal batteries coupling thin lithium metal anodes ($4\,mAh\,cm^{-2}$) and high-loading $LiNi_{0.8}Co_{0.15}Al_{0.05}O_2$ cathodes ($10\,mg\,cm^{-2}$) retain 70% of the initial capacity after 100 cycles at $-20°C$. These results, as a proof of concept, demonstrate the applicability of locally concentrated ionic liquid electrolytes for low-temperature lithium metal batteries.

Introduction

Lithium metal, exhibiting a high theoretical specific capacity ($3860\,mAh\,g^{-1}$) and low redox potential ($-3.04\,V$ vs. standard hydrogen electrode), is an ideal anode material for next-generation high-energy-density rechargeable batteries.[1] The low stripping/plating Coulombic efficiency (CE) and dendritic growth of lithium metal anodes (LMAs) are notorious issues hindering their practical applications.[2] Tremendous efforts have been devoted to mitigate the aforementioned issues, while most of them are conducted at room temperature.[3–5] When the operation temperature is decreased below zero, the slowed Li^+ transport in electrolytes,[6] increased barriers of Li^+ de-solvation process at electrolyte/electrode interfaces,[7] and the reduced protection of the solid electrolyte interphases (SEIs) formed on LMAs accelerate the growth of lithium dendrites and side reactions between lithium and the electrolytes.[8] This results in increased safety risk and shortened lifespan of LMBs. In fact, batteries that can charge and discharge at low temperatures, e.g., $-20°C$, are widely required even for civil use.[9–11]

Electrolyte engineering is one of the most relevant strategies in developing low-temperature, dendrite-free, and highly reversible LMAs, because electrolytes not only govern the Li^+ transport and de-solvation, but also affect the formation of the SEIs.[12,13] So far, a few electrolytes based on liquefied gas,[14,15] ether,[7,16] carbonate,[17,18] and/or acetate solvents with low freezing points have been reported for such a purpose.[19,20] It has also become clear that the solvation structure of Li^+ has significant influence on the low-temperature performance of LMAs.[7,13,21,22] Due to the electrostatic repulsion effect of negatively charged anodes on anions upon lithium plating, the Li^+ de-solvation process is mainly limited by the interaction between Li^+ and solvents, i.e., a Li^+ solvation shell consisting of anions rather than solvent molecules is beneficial for a more facile de-solvation process and consequently dendrite-free lithium stripping/plating.[7,13] Despite the progress, it has to be noted that most of the aforementioned electrolytes designed for low-temperature LMAs are highly flammable.

Room-temperature ionic liquids (RTILs) with non-volatility and high thermal stability are well-known solvents for poorly-flammable electrolytes, consisting of bulky organic cations and anions, e.g., the 1-ethyl-3-methylimidazolium cation ($Emim^+$) and bis(fluorosulfonyl)imide anion (FSI^-), respectively.[23,24] Due to the charge delocalization and/or steric hindrance, the bulky organic cations and anions coordinate weakly.[25] When lithium salts are dissolved in RTILs, Li^+ exhibiting smaller ionic radius and thereby higher Lewis acidity than the organic cations tightly coordinates with the negatively charged anions; meanwhile, the positively charged organic cations are repelled from the first salvation shell of Li^+.[26] Therefore, the solvation sheath of Li^+ in the ionic liquid electrolytes (ILEs) only consists of

[*] Dr. X. Liu, Dr. T. Diemant, Dr. X. Dong, P.-H. Su, Prof. S. Passerini
Helmholtz Institute Ulm (HIU) Electrochemical Energy Storage
Helmholtzstraße 11, 89081 Ulm (Germany)
and
Karlsruhe Institute of Technology (KIT)
P.O. Box 3640, 76021 Karlsruhe (Germany)
E-mail: stefano.passerini@kit.edu

Dr. A. Mariani
ELETTRA Sincrotrone Trieste
Basovizza, 34012 Trieste (Italy)

Prof. S. Passerini
Chemistry Department,
Sapienza University of Rome
Piazzale Aldo Moro 5, 00185 Rome (Italy)

anions, which is desired for the Li stripping/plating at low temperatures as mentioned before. On the other hand, ILEs suffer from sluggish Li^+ transport even at room temperature because of their high viscosity, which becomes even worse at decreased temperatures.[27] For this reason, ILEs are seldom considered for sub-zero LMBs. Recently, diluting ILEs with low-viscosity and non-solvating co-solvents to form locally concentrated ionic liquid electrolytes (LCILEs) was proven to be an effective approach in promoting Li^+ transport without significantly affecting the unique, anion-dominating solvation of Li^+ in ILEs,[28–31] which is inspired by a similar approach for organic-solvent-based concentrated electrolytes.[32–36] In this context, LCILEs are interesting candidates for low-temperature LMBs, but have not been investigated yet. Whether the unique Li^+ solvation and solution structure are maintained at low temperatures and how LMAs behave in LCILEs at low temperatures remain unknown to date.

Herein, the state-of-the-art LCILE consisting of LiFSI, EmimFSI, and 1,2-difluorobenzene (dFBn) in a molar ratio of 1:2:2, i.e., $[LiFSI]_1[EmimFSI]_2[dFBn]_2$ (FEdF),[37] and the neat ILE, i.e., $[LiFSI]_1[EmimFSI]_2$ (FE), are selected as model electrolytes to evaluate the compatibility of LCILEs toward LMAs and the influence of the non-solvating co-solvent on the properties of LMAs at low temperatures. It is anticipated that the LMB employing the neat ILE cannot operate at $-20\,°C$ even with a low current density of $0.1\,mA\,cm^{-2}$. On the other hand, the FEdF shows a thoroughly improved ionic transport at the same temperature, enabling lithium stripping/plating at current densities up to $0.5\,mA\,cm^{-2}$, benefiting from the well maintained Li^+ solvation and solution structure. Moreover, FEdF offers a lithium stripping/plating CE of 98.3% and dendrite-free cycling of Li/Li cells up to 1600 h at $-20\,°C$, which results also from the SEI rich in inorganic compounds. Furthermore, FEdF shows high compatibility with the high-voltage $LiNi_{0.8}Co_{0.15}Al_{0.05}O_2$ (NCA) cathode at $-20\,°C$. With further optimization of the electrolyte components, lithium stripping/plating efficiency of 98.9% has been achieved at $-20\,°C$.

Results and Discussion

Flash points of the electrolytes were measured to evaluate their flammability. Due to the non-volatility and high thermal stability, no flash was detected for FE in the temperature range of 25–300°C. The addition of volatile dFBn with a flash point of 1°C leads to the occurrence of a flash at 114°C for FEdF, due to the increased vapor pressure of the ternary mixture with respect to FE.[38] Since the American Occupational Safety and Health Standards define liquids with a flashpoint at or below 93°C as flammable,[39] FEdF can be classified to have a low flammability.

Freezing of electrolytes is one of the problems causing the poor electrochemical performance at low temperatures, leading to low ionic conductivities.[6,19] Differential scanning calorimetry (DSC) measurements were conducted to investigate the thermal properties of the electrolytes. As shown

in Figure 1a, the melting temperatures (T_m) of EmimFSI and dFBn are -14.3 and $-48.0\,°C$, respectively. When LiFSI is added to EmimFSI with a molar ratio of 1:2, the mixture, i.e., FE, exhibits no T_m point but a glass transition (T_g) at $-85.6\,°C$. The T_g of FEdF is observed at even lower temperature, i.e., $-90.6\,°C$. Taken together, the results demonstrate that both FE and FEdF are liquid in a wide temperature range. The ionic conductivity of FE and FEdF was measured in the temperature range from $-40\,°C$ to $50\,°C$. In general, FEdF exhibits higher ionic conductivity than FE as shown in Figure 1b, supporting for a superior ionic transport. For instance, the ionic conductivities of FE and FEdF at $-20\,°C$ are 0.50 and $1.67\,mS\,cm^{-1}$, respectively. These results imply the possible use of FEdF as an electrolyte for low-temperature batteries.

As mentioned, the structure of the electrolytes, particularly the local solvation of Li^+, is important for dendrite-free lithium stripping/plating at low temperatures.[7,13] Therefore, Raman spectroscopy was used to resolve the coordination of FSI^- with Li^+ in FE and FEdF in the temperature range from -40 to $40\,°C$. The commonly used ν_s(S–N–S) mode of FSI^- in the region of $700–770\,cm^{-1}$ overlaps with the signals from $Emim^+$ and dFBn.[37] However, the $\nu_s(SO_2)$ mode of FSI^- does not suffer of any interference and, thus, was selected for the analysis. Neat EmimFSI exhibits a peak at $1217.2\,cm^{-1}$ without any shift from -20 to $40\,°C$ (Figure 2a). The peak originates from "free" FSI^- only weakly coordinating to the bulky $Emim^+$. At $-40\,°C$, this peak slightly shifts to $1215.4\,cm^{-1}$, due to the freezing of EmimFSI. Compared with pure EmimFSI, broader peaks at higher wavenumber are detected for FE and FEdF (Figure 2b and S1a, respectively). These changes can be attributed to the coordination of FSI^- to Li^+. Furthermore, it is also observed that the peak shifts successively to higher wavenumber with decreasing temperature for both electrolytes, indicating that more FSI^- participates in the solvation of Li^+ at lower temperatures. For instance, Figure 2c shows the fitting analysis of this peak for FEdF at 20°C and $-20\,°C$. The fraction of Li^+-coordinated FSI^- is 71.5% and 76.3% at 20°C and $-20\,°C$, respectively. Therefore, the full-anion solvation sheath of Li^+ in FEdF is not affected in the examined temperature range.

The structure of FEdF at a larger scale was evaluated via small- and wide-angle X-ray scattering (SWAXS), as shown
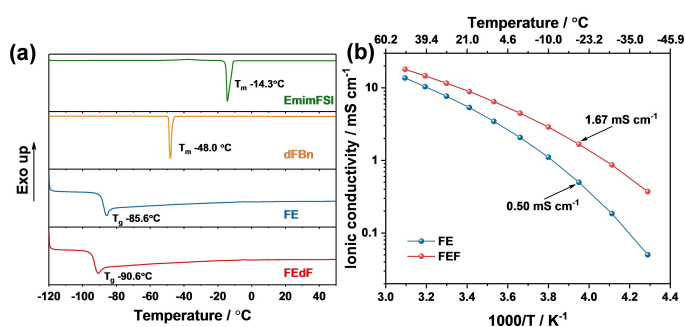
Figure 1. a) DSC thermograms of EmimFSI, dFBn, FE, and FEdF. b) Ionic conductivity of FE and FEdF at various temperatures.
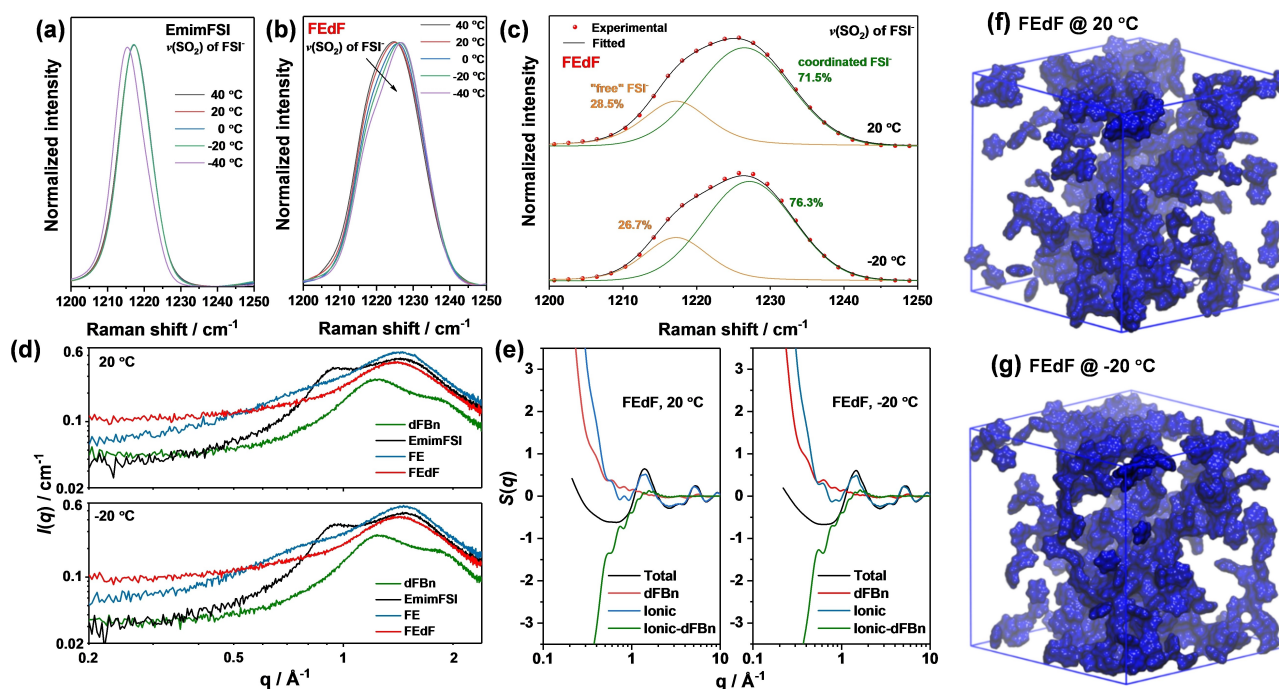
Figure 2. Raman spectra of a) EmimFSI and b) FEdF in the region corresponding to the $\nu_s(SO_2)$ mode of FSI$^-$ measured in the temperature range from 40 to $-40\,°C$. c) Fitting analysis of the Raman spectra of FEdF at $20\,°C$ and $-20\,°C$. The "free" FSI$^-$ corresponds to FSI$^-$ weakly coordinating to Emim$^+$. d) Experimental SWAXS patterns collected at $20\,°C$ (top) and $-20\,°C$ (bottom). e) Computed SWAXS patterns and corresponding partial structure factors for the simulations at $20\,°C$ (left) and $-20\,°C$ (right). Snapshots of the simulation boxes of FEdF at f) $20\,°C$ and g) $-20\,°C$. Both boxes have a side length of ≈ 60 Å. The empty space and the blue part represent the ionic portion and dFBn of the system, respectively.

in Figure 2d. Peaks locating between 0.7 and 1.0 Å^{-1} were observed from the pattern of IL-based samples, associated with distances between ions of similar charge, e.g., the distance between two cations mediated by an anion, and vice versa.[40] The main peak around 1.4 Å^{-1} is associated with the first neighbor's interaction and gives the structural information on the adjacent species' average distance.[41] More importantly, the collected SWAXS patterns clearly display the low-q-excess (LqE) phenomenon, which manifests in an enhanced scattering intensity at small angles, i.e., at q values smaller than 0.5 Å^{-1} in this specific case. Specifically, the term LqE is used for complex mixtures showing more intensity in the low-q scattering region than any of the mixture's components. When the system is made exclusively of small molecules, LqE can only originate from the so-called phase-nano-segregation,[42] i.e., the formation of nanometer-sized regions of de-mixing being thermodynamically stable, but not affecting the system macroscopically.[43–47] This observation is in line with what was previously reported,[37,48] but this is the first direct evidence for the formation of large-scale density fluctuations in LCILEs, to the best of our knowledge.

LqE is observed in both the FE and FEdF systems but is more intense in the latter. Such a behavior can be explained by the formation of Li$^+$-FSI$^-$ clusters in both systems and additional dFBn domains in FEdF. A change in temperature does not induce any major difference in the overall structure of the system (Figure S2), demonstrating that the bulk

structure of FEdF is maintained even at $-20\,°C$, allowing it to be used in such extreme conditions.

To confirm the interpretation, MD simulations were conducted, and the structure factor was calculated with the TRAVIS software.[49,50] The advantage of the model is that specific contributions to the overall structure factor can be selected. The structure factor $S(q)$ is defined by:

$$S(q) = \frac{\sum_{i \neq j} x_i \cdot f_i \cdot x_j \cdot f_j \cdot H_{i,j}(q)}{\sum_{i \neq j} x_i \cdot f_i^2 \cdot x_j \cdot f_j^2} - 1 \tag{1}$$

where every i-j atom pair has the respective mole fractions x_i and x_j, the atomic form factors f_i and f_j, and the Fourier transform of their radial distribution function $H_{i,j}(q)$. As evident from Equation (1), it is possible to isolate the partial structure functions by selecting only a subset of the possible i and j pairs.

It should be mentioned that such partial structure factors, $S_{i,j}(q)$, are not accessible experimentally with X-ray scattering since it is not possible to mask atoms experimentally. In the case of computational modelling, the atom pair selection is straightforwardly made by setting the mole fraction of the undesired atoms to zero in Equation (1), as implemented in the TRAVIS software. Practically, this is equivalent to make the undesired atoms transparent to X-rays, thus observing only the scattering pattern originating from the selected atoms in their positions. The total $S(q)$ was separated into three partial $S_{i,j}(q)$, namely $S_{dFBn}(q)$ (with contributions only from dFBn molecules), $S_{Ionic}(q)$ (with

contributions from the ionic species, i.e., Li^+, $Emim^+$, and FSI^-), and the cross-term $S_{Ionic\_dFBn}(q)$, i.e., total $S(q)$ with the contributions from ionic-ionic and dFBn-dFBn removed. The results are depicted in Figure 2e; the left and right panels correspond to the simulations at 20 °C and −20 °C, respectively. It must be mentioned that MD simulations are performed in boxes which are (albeit big) much smaller than the real systems, and that the LqE size is at the limit of what is possible to obtain from an MD simulation in a reasonable time. Nonetheless, as already established in the literature,[42,44] it is possible to extract useful information about highly inhomogeneous systems from such models. Herein, the total $S(q)$ (black curves in Figure 2e) clearly show an upward trend toward the low-q limit; hence, the simulation can reproduce the formation of LqE. In the LqE region, an intense positive contribution coming from both the $S_{dFBn}(q)$ and the $S_{Ionic}(q)$ can be observed, meaning that the scattering objects are made by dFBn and Li^+-FSI^--$Emim^+$ domains. Additionally, and most importantly, a large negative contribution from the cross-term $S_{Ionic\_dFBn}(q)$ is present. A negative contribution in a partial $S(q)$ (the so-called "anti-peak") means that there is an anti-correlation between the species considered in the partial structure factor, i.e., the species considered are mutually excluded at that specific characteristic distance.[51] Therefore, the overall picture of the bulk system consists of two percolating regions consisting of dFBn and ionic species, as clearly seen from the simulation box snapshots in Figure 2f, g, where the empty space and the blue part represent, respectively, the ionic and dFBn portions of the system. Calculated by means

of Voronoi tessellation as implemented in Travis,[52] the volume fraction occupied by dFBn is 27.492 % and 27.205 % at 20 and −20 °C, respectively, which demonstrates the negligible effect of the temperature decrease from 20 to −20 °C on the solution structure. Additionally, the low volume percentage of dFBn in the electrolyte indicates that the ionic network still dominates the electrolyte, based on which one can infer that the Li^+ diffusivity is more facile to occur in the continuous ionic network. Once again, it is important to note that the system appears macroscopically as a single phase and completely transparent. The electrolyte model does not show any difference at 20 °C and −20 °C, hinting at the possibility to use it as an electrolyte at sub-zero temperatures.

Li/Li symmetric cells were assembled to evaluate the rate capability of LMAs in FE and FEdF at −20 °C. The areal capacity for each stripping or plating process was set to 1 mAh cm^{-2}, while the current density was increased step-wise from 0.1 to 0.5 mA cm^{-2}. As shown in Figure 3a, a short circuit occurred in the Li/FE/Li cell already at 0.1 mA cm^{-2}, due to the sluggish Li^+ transport in FE, particularly at such a low temperature. In contrast, Li/FEdF/Li survived up to 0.5 mA cm^{-2} with an average voltage plateau of 0.152 V, as displayed in Figure 3b and Figure S3. Dendrite-free deposition was observed for the lithium (1.5 mAh cm^{-2}) deposited on Cu foil at 0.2 mA cm^{-2} via scanning electron microscopy (SEM), as shown in Figure S4. The lithium stripping/plating CE in FEdF at 0.2 mA cm^{-2} was measured to be 98.3 % via the cycling of lithium metal deposited on Cu (Figure 3c). To assess the long-term cyclability, Li/Li symmetric cells were
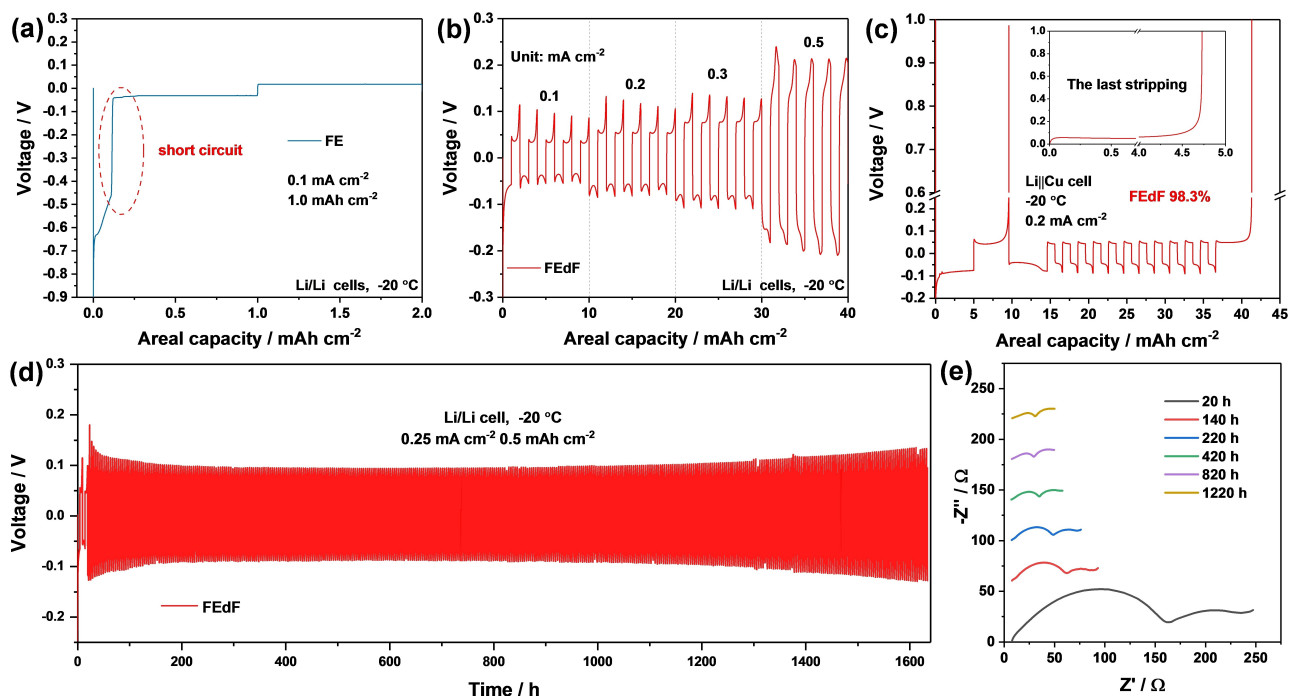
Figure 3. Electrochemical performance of LMAs in FE and FEdF at −20 °C. a) Voltage profile of a Li/FE/Li cell upon plating/stripping at 0.1 mA cm^{-2}. b) Voltage profile of a Li/FEdF/Li cell upon plating/stripping at various current densities. c) Voltage profile of a Li/FEDF/Cu cell upon Li plating/stripping at 0.2 mA cm^{-2}. d) Voltage profile of a Li/FEdF/Li cell upon long-term, galvanostatic plating/stripping cycling test. e) Nyquist plots from EIS measurements on the Li/FEdF/Li cell upon long-term cycling.

assembled and cycled at −20°C with a cycling capacity of 0.5 mAh cm^{-2}. After two formation cycles at 0.1 mA cm^{-2}, 0.25 mA cm^{-2} were applied for the following cycling. As shown in Figure 3d, a decrease of overvoltage was observed in the initial 25 cycles, after which stable overvoltage was maintained for more than 1000 h. Voltage profiles at selected cycles are shown in Figure S5. The Nyquist plots of the cell after different Li stripping/plating cycles are shown in Figure 3e. The high-frequency intercept did not change upon cycling, excluding the severe electrolyte's degradation. Besides, the depressed semicircles at lower frequencies associated to the interfacial resistance decreased in the initial 50 cycles before reaching the steady state,[53,54] which is identical to the decreased overvoltage in the initial cycling. This can be explained by the reconstruction of LMAs' native SEI mainly consisting of Li$_2$O to newly generated SEI via the decomposition of the electrolyte.[55,56] Once this process is completed, the stable and low-impedance SEI enables robust cycling of LMAs with lower overpotential. In general, the electrochemical results demonstrate the feasibility of lithium stripping/plating at low temperatures in LCILEs.

The surface morphology of LMAs at the pristine state and after 50 cycles is shown by the SEM images in Figure 4a and b, respectively. The typical texture of lithium foil was observed for the pristine LMA (Figure 4a). Due to the repeated stripping and plating of lithium, the surface morphology significantly changed during cycling (Figure 4b). Nonetheless, the LMA still kept a dense and dendrite-free morphology after cycling, which promotes the cyclability of LMAs. Figure 4c displays a cross-sectional SEM image of

the cycled LMAs. The thickness of the corrosion layer formed on the surface of LMAs due to the repeated stripping/plating of lithium metal was only 33 μm.

To shed light on the composition of the generated SEI on LMAs in FEdF at the low temperature, XPS measurements were acquired on a LMA after cycling in FEdF. The results obtained before and after Ar$^+$ sputtering are shown in Figure 4d. Considering the electrode's surface first, one can observe four peaks in the N 1s spectrum. The peaks at 401.8 and 399.7 eV result from the positively charged nitrogen atoms (N$_{cation}$) from Emim$^+$ and negatively charged nitrogen atoms (N$_{anion}$) from FSI$^-$, respectively.[57] The peak (N$_{dec}$) at 398.4 eV is associated with the incomplete decomposition of Emim$^+$ and FSI$^-$,[58,59] while complete decomposition leads to the formation of Li$_3$N, which correlates to the peak at 396.4 eV.[60] The presence of N$_{cation}$ and N$_{anion}$ demonstrates that both Emim$^+$ and FSI$^-$ participate in the formation of the SEI. In the S 2p spectra, a multitude of sulfur species with S 2p3/2 peaks at 170.0, 168.6, 166.6, 164.1, 161.9, and 160.0 eV was observed, which can be assigned to sulfur in FSI$^-$, sulfate, sulfite, S–S bond, Li$_2$S$_2$, and Li$_2$S, respectively.[61,62] Since FSI$^-$ is the only sulfur-containing species in the electrolyte, these sulfur-based SEI components can be unambiguously attributed to the deposition and decomposition of FSI$^-$.

In the C 1s spectra, the main peak located at 284.8 eV reflects the C–C/C=C bond. The peak at 282.2 eV is assigned to Li–C species generated via the decomposition of Emim$^+$.[63] The signal of C–N and C–O bonds overlaps and gives rise to the peak at 286.4 eV.[57,58] The other peak at the
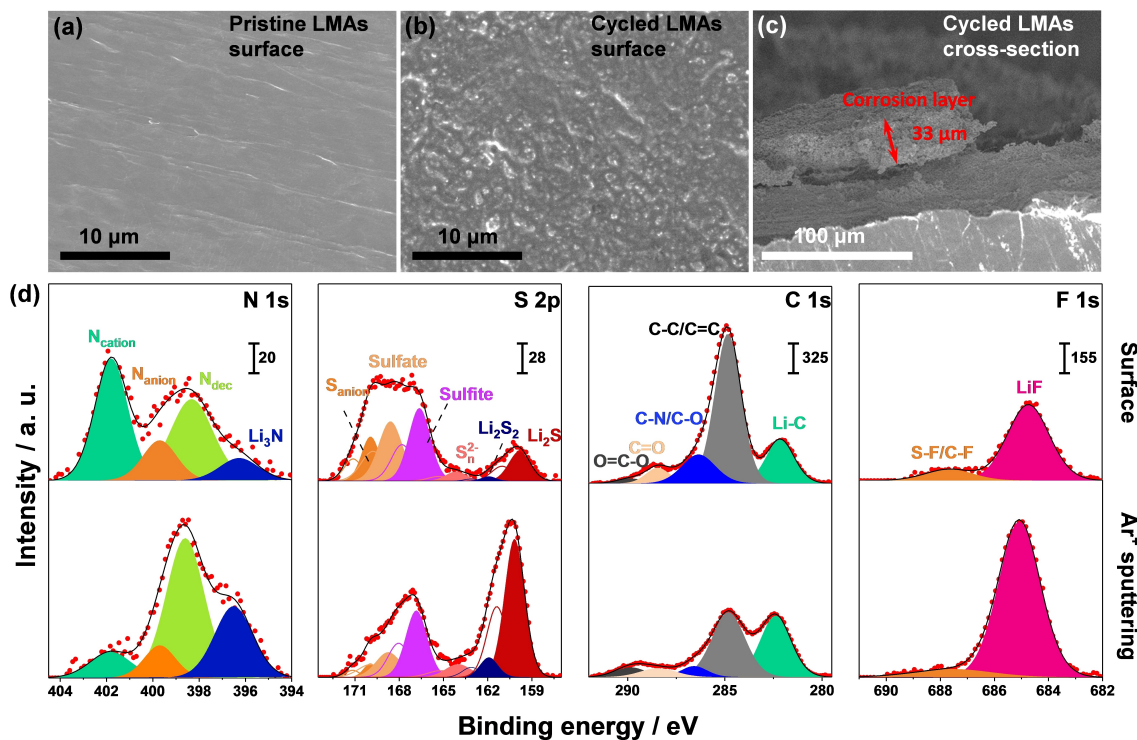
Figure 4. SEM images of a) pristine Li foil and (b, c) LMA after 50 stripping/plating cycles in FEdF at −20°C. d) XPS spectra of the cycled LMA before and after Ar$^+$ sputtering.

binding energy of 288.4 eV can be attributed to the C=O species.[62] It is noticed that the area of the C–C/C=C peak is four times that of the C–N/C–O peak, while the elemental ratio between carbon and nitrogen of Emim$^+$ is only 3:1. Therefore, decomposition products of dFBn with high carbon content also join the formation of SEI and contribute to the C–C/C=C peak in the C 1s spectra. In the F 1s spectra, the peak around 685.0 eV represents LiF generated from FSI$^-$ and dFBn,[62] while the peak at 687.7 eV can be assigned to S–F and C–F of the deposited and incompletely decomposed FSI$^-$ and dFBn, respectively.[58]

After Ar$^+$ sputtering, all the above-mentioned SEI species were still observed, but with significantly changed concentrations. The C–N/C–O (C 1s), C–C/C=C (C 1s), and N$_{cation}$ (N 1s) peaks decreased in intensity, implying reduced contributions of Emim$^+$ and dFBn. Meanwhile, the peaks of LiF (F 1s), Li$_3$N (N 1s), Li$_2$S$_2$ (S 2p), and Li$_2$S (S 2p) got more pronounced, demonstrating a larger contribution from the FSI$^-$ decomposition going deeper in the SEI layer. These inorganic species with poor electronic transport and high mechanical strength are known to suppress side reactions between LMAs and electrolytes as well as the lithium dendrite growth, yielding high lithium stripping/plating CE.[21,64]

The compatibility of the electrolyte towards nickel-rich cathode at −20 °C was evaluated using Li/NCA coin cells within the 2.8–4.4 V voltage window. In a first step, electro-des with a moderate NCA loading (2.7 mg cm^{-2}) and thick lithium foils (500 μm) were used. The amount of the electrolyte added to each cell was 75 μL.

Figure 5a shows the voltage profile of the initial dis-/charge cycle at 0.1 C of Li/NCA cells employing FE and FEdF electrolytes. With the latter electrolyte, the charge and discharge specific capacity was 217 and 162 mAh g^{-1}, respectively, corresponding to a CE of 74.65 %. This value is lower than that obtained at 20 °C, i.e., 88.3 % (Figure S6), which can be attributed to the slow lithiation kinetics of NCA at high lithium contents and low temperatures.[65] After the initial cycle, highly reversible dis-/charge (CE > 99.9 %) was achieved (Figure S7). For Li/NCA cells employing FE, a short circuit occurred in the initial charge and the cell failed for further operation, due to the limited Li$^+$ transport ability at such a low temperature. This result matches that of Li/FE/Li symmetric cells (see Figure 3a).

The Li/FEdF/NCA cell was then subjected to a rate capability test. As summarized in Figure 5b, the cell was capable to discharge at 1 C (200 mA g^{-1}, 0.54 mA cm^{-2}) with a promising specific capacity of 154 mAh g^{-1}, benefiting from the sufficient Li$^+$ transport in FEdF even at such a low temperature. The dis-/charge profiles at different current rates are shown in Figure S8. The long-term cyclability was evaluated with a charge rate of C/3 and a discharge rate of 1 C after two formation cycles at C/10. The evolution of discharge specific capacity and CE is summarized in Fig-
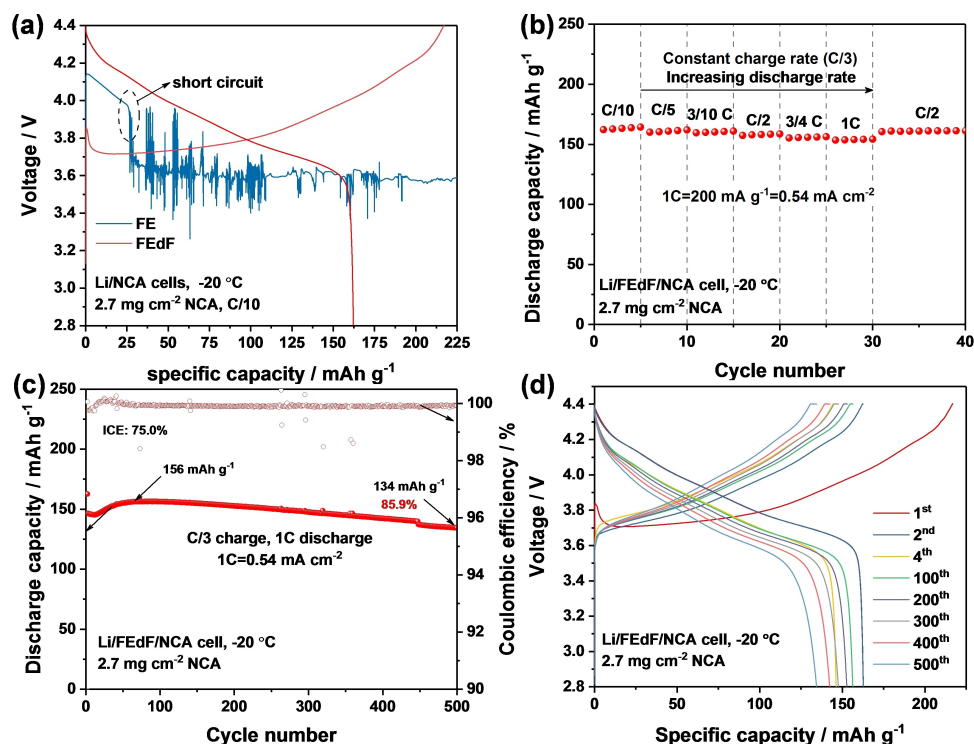
Figure 5. Electrochemical performance of Li/NCA (2.7 mg cm^{-2}) cells employing FE and FEdF electrolytes at −20 °C. a) Voltage profile of Li/NCA cells employing FE or FEdF electrolyte upon the first cycle with a current rate of C/10. b) Rate performance of a Li/FEdF/NCA cell at different discharge C-rates with a constant charge rate of C/3 after five formation cycles at C/10 (charge and discharge). c) Discharge specific capacity and CE evolution for a Li/FEdF/NCA cell upon long-term cycling at C/3 charge and 1 C discharge (after two formation cycles at C/10). d) Selected dis-/charge profiles upon long-term cycling. 1 C is 200 mA g^{-1} and corresponds to 0.54 mA cm^{-2}.
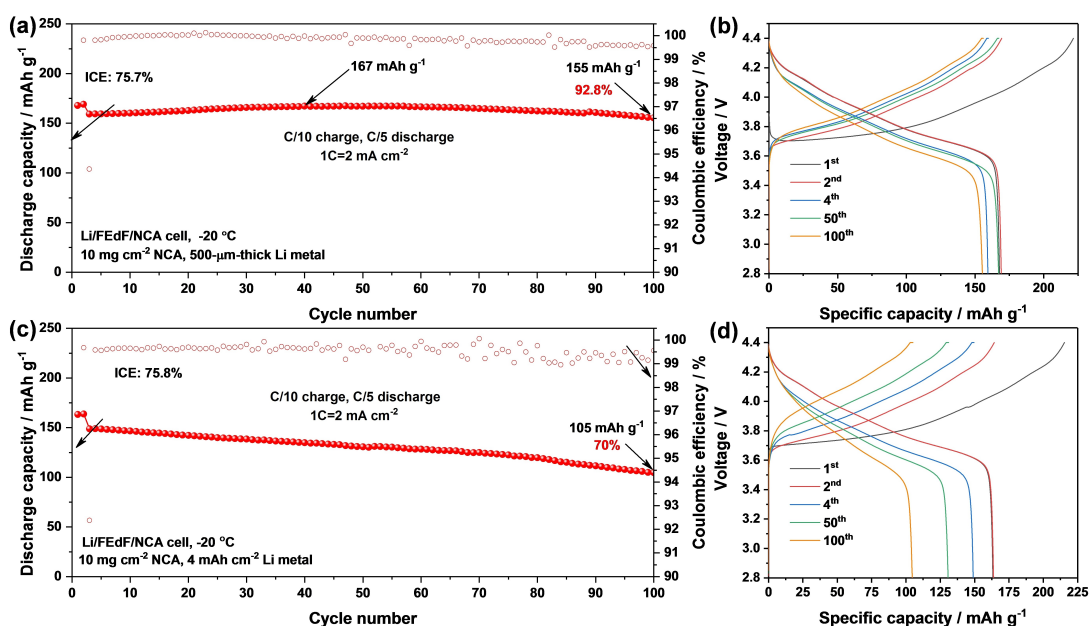
Figure 6. Cycling stability of Li/FEdF/NCA (10 mg cm^{-2}) cells employing a), b) 500-μm-thick or c), d) 20-μm-thick (4 mAh cm^{-2}) lithium metal anodes at −20 °C. a), c) The evolution of discharge specific capacity and CE upon cycling. b), d) Dis-/charge profiles of a few selected cycles in the cycling test. The cells were cycled at C/10 charge and C/5 discharge after two formation cycles at C/20. 1 C is 200 mA g^{-1}.

ure 5c, and the dis-/charge profiles at selected cycles upon cycling are displayed in Figure 5d. Due to the formation of a protective cathode/electrolyte interphase rich in fluorine (Figure S9, S10), the electrode exhibits an average CE of 99.9 % in the 4th–500th cycles and a capacity retention of 85.9 % after 500 cycles. These results demonstrate the high compatibility of the electrolyte towards nickel-rich layered oxides and the excellent performance even at such a low temperature.

In the next step, NCA electrodes with a higher areal loading (10 mg cm^{-2}) were employed. The Li/FEdF/NCA cells, assembled using 500-μm thick Li electrodes, were cycled with a charge rate of C/10 and a discharge rate of C/5 after two formation cycles at C/20. The evolution of discharge specific capacity and the dis-/charge profiles of a few selected cycles are shown in Figure 6a, b, respectively. The specific capacity in the formation cycles was 170 mAh g^{-1}, which decreased to 159 mAh g^{-1} in the third cycle with higher current rate. It gradually increased to 167 mAh g^{-1} around the 40th cycle, and finally arrived at 155 mAh g^{-1} in the 100th cycle, which corresponds to a remarkable capacity retention of 92.8 %. In a further step, Li/NCA cells were assembled coupling the high areal loading NCA positive electrodes (10 mg cm^{-2}) with low areal capacity (4 mAh cm^{-2}) lithium negative electrodes, exhibiting a negative to positive areal capacity (N/P) ratio of 1:2.35.

The electrolyte amount in these cells was decreased to 20 μL. The test results obtained using the same test protocol, are shown in Figure 6c, d. The cell delivered 149 mAh g^{-1} in the 3rd cycle and kept 70 % of the capacity after 100 cycles, which is inferior to the cell employing the 500-μm thick lithium foil. This capacity fading can be attributed to the still

limited CE (i.e., 98.3 %) of LMAs in the electrolyte and/or the lower amount of electrolytes in the cell. Nonetheless, as a proof of concept, these results demonstrate the feasibility of the use of LCILEs for low-temperature LMBs.

It should be noted that the stripping/plating CE of LMAs can be improved from 98.3 % to 98.9 % via optimizing the concentration of LiFSI, EmimFSI, and dFBn of FEdF (Figure S11). Further improvement of the reversibility of LMAs in this type of electrolytes can be expected via optimization of their formulation, particularly with regard to the vast choice of organic cations and anions for the ionic liquid component.[23,24]

Conclusion

We propose a poorly-flammable LCILE with a wide liquidus range and sufficient ionic transport at low temperatures, which can be used for low-temperature LMBs. The Li$^+$ solvation consisting of anions and the unique solution structure of phase-nano-segregation are not affected by the low temperatures (down to −20 °C), enabling a dendrite-free operation of LMAs at current densities up to 0.5 mA cm^{-2}. The anion-derived SEI is rich in inorganic compounds leading to highly reversible lithium stripping/plating at −20 °C. Benefiting from the sufficient Li$^+$ transport and highly reversible LMAs, stable cycling of cells with LMAs and NCA positive electrodes with areal loading of 10 mg cm^{-2} is possible. Moreover, the lithium stripping/plating can be further improved via rational optimization of the electrolyte composition. Overall, these results demonstrate the favourable use of LCILEs for low-temperature LMBs.

Supporting Information

Supporting Information is available from the internet or from the author.

Acknowledgements

Conflict of Interest

The authors declare no conflict of interest.

Data Availability Statement

The data that support the findings of this study are available on request from the corresponding author. The data are not publicly available due to privacy or ethical restrictions.

[1] X. He, D. Bresser, S. Passerini, F. Baakes, U. Krewer, J. Lopez, C. T. Mallia, Y. Shao-Horn, I. Cekic-Laskovic, S. Wiemers-Meyer, *Nat. Rev. Mater.* **2021**, *6*, 1036–1052.

[2] G. M. Hobold, J. Lopez, R. Guo, N. Minafra, A. Banerjee, Y. Shirley Meng, Y. Shao-Horn, B. M. Gallant, *Nat. Energy* **2021**, *6*, 951–960.

[3] J. Chen, Z. Li, N. Sun, J. Xu, Q. Li, X. Yao, J. Ming, Z. Peng, *ACS Energy Lett.* **2022**, *7*, 1594–1603.

[4] M. Wan, S. Kang, L. Wang, H. W. Lee, G. W. Zheng, Y. Cui, Y. Sun, *Nat. Commun.* **2020**, *11*, 829.

[5] X. Liang, Q. Pang, I. R. Kochetkov, M. S. Sempere, H. Huang, X. Sun, L. F. Nazar, *Nat. Energy* **2017**, *2*, 17119.

[6] A. C. Thenuwara, P. P. Shetty, M. T. McDowell, *Nano Lett.* **2019**, *19*, 8664–8672.

[7] J. Holoubek, H. Liu, Z. Wu, Y. Yin, X. Xing, G. Cai, S. Yu, H. Zhou, T. A. Pascal, Z. Chen, *Nat. Energy* **2021**, *6*, 303–313.

[8] Y. Gao, T. Rojas, K. Wang, S. Liu, D. Wang, T. Chen, H. Wang, A. T. Ngo, D. Wang, *Nat. Energy* **2020**, *5*, 534–542.

[9] N. Zhang, T. Deng, S. Zhang, C. Wang, L. Chen, C. Wang, X. Fan, *Adv. Mater.* **2022**, *34*, 2107899.

[10] Y. Feng, L. Zhou, H. Ma, Z. Wu, Q. Zhao, H. Li, K. Zhang, J. Chen, *Energy Environ. Sci.* **2022**, *15*, 1711–1759.

[11] A. Gupta, A. Manthiram, *Adv. Energy Mater.* **2020**, *10*, 2001972.

[12] X. Fan, X. Ji, L. Chen, J. Chen, T. Deng, F. Han, J. Yue, N. Piao, R. Wang, X. Zhou, *Nat. Energy* **2019**, *4*, 882–890.

[13] J. Holoubek, K. Kim, Y. Yin, Z. Wu, H. Liu, M. Li, A. Chen, H. Gao, G. Cai, T. A. Pascal, *Energy Environ. Sci.* **2022**, *15*, 1647–1658.

[14] Y. Yang, D. M. Davies, Y. Yin, O. Borodin, J. Z. Lee, C. Fang, M. Olguin, Y. Zhang, E. S. Sablina, X. Wang, *Joule* **2019**, *3*, 1986–2000.

[15] Y. Yang, Y. Yin, D. M. Davies, M. Zhang, M. Mayer, Y. Zhang, E. S. Sablina, S. Wang, J. Z. Lee, O. Borodin, *Energy Environ. Sci.* **2020**, *13*, 2209–2219.

[16] H. Jiang, C. Yang, M. Chen, X. Liu, L. Yin, Y. You, J. Lu, *Angew. Chem. Int. Ed.* **2023**, *62*, e202300238.

[17] J. Holoubek, M. Yu, S. Yu, M. Li, Z. Wu, D. Xia, P. Bhaladhare, M. S. Gonzalez, T. A. Pascal, P. Liu, *ACS Energy Lett.* **2020**, *5*, 1438–1447.

[18] Z. Wang, Z. Sun, Y. Shi, F. Qi, X. Gao, H. Yang, H. Cheng, F. Li, *Adv. Energy Mater.* **2021**, *11*, 2100935.

[19] X. Dong, Y. Lin, P. Li, Y. Ma, J. Huang, D. Bin, Y. Wang, Y. Qi, Y. Xia, *Angew. Chem. Int. Ed.* **2019**, *58*, 5623–5627.

[20] N. Kim, Y. Myung, H. Kang, J. W. Lee, M. Yang, *ACS Appl. Mater. Interfaces* **2019**, *11*, 33844–33849.

[21] J. Shi, C. Xu, J. Lai, Z. Li, Y. Zhang, Y. Liu, K. Ding, Y. P. Cai, R. Shang, Q. Zheng, *Angew. Chem. Int. Ed.* **2023**, *62*, e202218151.

[22] T. Ma, Y. Ni, Q. Wang, W. Zhang, S. Jin, S. Zheng, X. Yang, Y. Hou, Z. Tao, J. Chen, *Angew. Chem. Int. Ed.* **2022**, *61*, e202207927.

[23] D. R. MacFarlane, M. Forsyth, P. C. Howlett, M. Kar, S. Passerini, J. M. Pringle, H. Ohno, M. Watanabe, F. Yan, W. Zheng, *Nat. Rev. Mater.* **2016**, *1*, 15005.

[24] X. Tang, S. Lv, K. Jiang, G. Zhou, X. Liu, *J. Power Sources* **2022**, *542*, 231792.

[25] O. Borodin, W. Gorecki, G. D. Smith, M. Armand, *J. Phys. Chem. B* **2010**, *114*, 6786–6798.

[26] H. Yoon, A. S. Best, M. Forsyth, D. R. MacFarlane, P. C. Howlett, *Phys. Chem. Chem. Phys.* **2015**, *17*, 4656–4663.

[27] U. Pal, D. Rakov, B. Lu, B. Sayahpour, F. Chen, B. Roy, D. R. MacFarlane, M. Armand, P. C. Howlett, Y. S. Meng, *Energy Environ. Sci.* **2022**, *15*, 1907–1919.

[28] X. Liu, A. Mariani, H. Adenusi, S. Passerini, *Angew. Chem. Int. Ed.* **2023**, *62*, e202219318.

[29] S. Lee, K. Park, B. Koo, C. Park, M. Jang, H. Lee, H. Lee, *Adv. Funct. Mater.* **2020**, *30*, 2003132.

[30] Z. Wang, F. Zhang, Y. Sun, L. Zheng, Y. Shen, D. Fu, W. Li, A. Pan, L. Wang, J. Xu, *Adv. Energy Mater.* **2021**, *11*, 2003752.

[31] Y. Cai, Q. Zhang, Y. Lu, Z. Hao, Y. Ni, J. Chen, *Angew. Chem. Int. Ed.* **2021**, *60*, 25973–25980.

[32] X. Cao, H. Jia, W. Xu, J.-G. Zhang, *J. Electrochem. Soc.* **2021**, *168*, 010522.

[33] Z. Jiang, Z. Zeng, X. Liang, L. Yang, W. Hu, C. Zhang, Z. Han, J. Feng, J. Xie, *Adv. Funct. Mater.* **2021**, *31*, 2005991.

[34] D. J. Yoo, S. Yang, K. J. Kim, J. W. Choi, *Angew. Chem. Int. Ed.* **2020**, *59*, 14869–14876.

[35] Z. Wu, R. Li, S. Zhang, L. lv, T. Deng, H. Zhang, R. Zhang, J. Liu, S. Ding, L. Fan, *Chem* **2023**, *9*, 650–664.

[36] L. Tan, S. Chen, Y. Chen, J. Fan, D. Ruan, Q. Nian, L. Chen, S. Jiao, X. Ren, *Angew. Chem. Int. Ed.* **2022**, *61*, e202203693.

[37] X. Liu, A. Mariani, T. Diemant, M. E. Di Pietro, X. Dong, M. Kuenzel, A. Mele, S. Passerini, *Adv. Energy Mater.* **2022**, *12*, 2200862.

[38] S. P. Verevkin, E. Safarov, E. Bich, E. Hassel, A. Heintz, *Fluid Phase Equilib.* **2005**, *236*, 222–228.

[39] American Occupational Safety and Health Standards, from https://www.osha.gov/laws-regs/regulations/standardnumber/1910/1910.106.

[40] L. Aguilera, J. Völkner, A. Labrador, A. Matic, *Phys. Chem. Chem. Phys.* **2015**, *17*, 27082–27087.

[41] X. Liu, M. Zarrabeitia, A. Mariani, X. Gao, H. M. Schütz, S. Fang, T. Bizien, G. A. Elia, S. Passerini, *Small Methods* **2021**, *5*, 2100168.

[42] A. Joseph, S. Mathew, *Theoretical and Computational Approaches to Predicting Ionic Liquid Properties*, Elsevier, Amsterdam, **2020**.

[43] A. Mariani, R. Caminiti, F. Ramondo, G. Salvitti, F. Mocci, L. Gontrani, *J. Phys. Chem. Lett.* **2017**, *8*, 3512–3522.

[44] A. Mariani, R. Dattani, R. Caminiti, L. Gontrani, *J. Phys. Chem. B* **2016**, *120*, 10540–10546.

[45] M. Campetella, A. Mariani, C. Sadun, B. Wu, E. W. Castner, L. Gontrani, *J. Chem. Phys.* **2018**, *148*, 134507.

[46] A. Mariani, M. Bonomo, B. Wu, B. Centrella, D. Dini, E. W. Castner, L. Gontrani, *Phys. Chem. Chem. Phys.* **2017**, *19*, 27212–27220.

[47] O. Russina, A. Sferrazza, R. Caminiti, A. Triolo, *J. Phys. Chem. Lett.* **2014**, *5*, 1738–1742.

[48] X. Liu, A. Mariani, M. Zarrabeitia, M. E. Di Pietro, X. Dong, G. A. Elia, A. Mele, S. Passerini, *Energy Storage Mater.* **2022**, *44*, 370–378.

[49] M. Brehm, M. Thomas, S. Gehrke, B. Kirchner, *J. Chem. Phys.* **2020**, *152*, 164105.

[50] M. Brehm, B. Kirchner, *J. Chem. Inf. Model.* **2011**, *51*, 2007–2023.

[51] H. K. Kashyap, J. J. Hettige, H. V. R. Annapureddy, C. J. Margulis, *Chem. Commun.* **2012**, *48*, 5103–5105.

[52] M. Brehm, H. Weber, M. Thomas, O. Hollóczki, B. Kirchner, *ChemPhysChem* **2015**, *16*, 3271–3277.

[53] L. Yu, S. Chen, H. Lee, L. Zhang, M. H. Engelhard, Q. Li, S. Jiao, J. Liu, W. Xu, J. G. Zhang, *ACS Energy Lett.* **2018**, *3*, 2059–2067.

[54] J.-J. Woo, V. A. Maroni, G. Liu, J. T. Vaughey, D. J. Gosztola, K. Amine, Z. Zhang, *J. Electrochem. Soc.* **2014**, *161*, A827–A830.

[55] A. Etxebarria, S. L. Koch, O. Bondarchuk, S. Passerini, G. Teobaldi, M. Á. Muñoz-Márquez, *Adv. Energy Mater.* **2020**, *10*, 2000520.

[56] M. Baek, J. Kim, K. Jeong, S. Yang, H. Kim, J. Lee, M. Kim, K. J. Kim, J. W. Choi, *Nat. Commun.* **2023**, *14*, 1296.

[57] M. Olschewski, R. Gustus, O. Höfft, A. Lahiri, F. Endres, *J. Phys. Chem. C* **2017**, *121*, 2675–2682.

[58] M. Olschewski, R. Gustus, M. Marschewski, O. Höfft, F. Endres, *Phys. Chem. Chem. Phys.* **2014**, *16*, 25969–25977.

[59] S. Liu, X. Ji, N. Piao, J. Chen, N. Eidson, J. Xu, P. Wang, L. Chen, J. Zhang, T. Deng, *Angew. Chem. Int. Ed.* **2021**, *60*, 3661–3671.

[60] K. Park, B. C. Yu, J. B. Goodenough, *Adv. Energy Mater.* **2016**, *6*, 1502534.

[61] G. G. Eshetu, T. Diemant, M. Hekmatfar, S. Grugeon, R. J. Behm, S. Laruelle, M. Armand, S. Passerini, *Nano Energy* **2019**, *55*, 327–340.

[62] J. F. Moulder, W. F. Stickle, P. E. Sobol, K. D. Bomben, *Handbook of X-ray Photoelectron Spectroscopy*, Physical Electronics, Feldkirchen, **1995**.

[63] G. F. Meyers, M. B. Hall, J. W. Chinn, R. J. Lagow, *J. Am. Chem. Soc.* **1985**, *107*, 1413–1414.

[64] A. C. Thenuwara, P. P. Shetty, N. Kondekar, S. E. Sandoval, K. Cavallaro, R. May, C. T. Yang, L. E. Marbella, Y. Qi, M. T. McDowell, *ACS Energy Lett.* **2020**, *5*, 2411–2420.

[65] H. Zhou, F. Xin, B. Pei, M. S. Whittingham, *ACS Energy Lett.* **2019**, *4*, 1902–1906.